https://ntrs.nasa.gov/search.jsp?R=20180005242 2019-05-01T03:01:31+00:00Z

Green's Function Applicable to Turbofan Exhaust Noise in Jets with an External Center-Body

Abbas Khavaran
Science Applications International Corporation
NASA Glenn Research Center, Cleveland, OH 44135
(abbas.khavaran@nasa.gov)

Abstract

The problem of propagation of sound across the shear layer in a turbofan jet exhaust with an external center-body is discussed. The wave equation of interest is the compressible Rayleigh equation. Two forms of the equation are considered, and the Green's function solutions, subject to appropriate surface conditions on the center-body and flight condition in the ambient, are presented. Directivity studies in a heated exhaust at temperature ratio of 2.0 and Mach number 0.90 indicate that a rigid center-body tends to increase the sound propagation at forward angles relative to an exhaust without a center-body, while application of suitable surface liner may significantly reduce this enhancement.

1. Introduction

EQUATIONS that govern the aerodynamic sound in a high-speed jet exhaust, when scrutinized in the context of Goldstein[1,2] generalized acoustic analogy, are obtained by writing the Navier-Stokes equations as a set of base flow equations, plus a set of five linear equations for fluctuating components of motion – called residual equations. By assuming the base flow (which is taken as the mean flow) as locally parallel, the factors on the operator side of the momentum and energy equations that explicitly depend on viscous stresses reduce to higher order terms and are neglected. The residual equations for continuity, momentum, and energy are then combined to construct a wave equation for pressure fluctuations (inhomogeneous Rayleigh equation), that is commonly used in acoustic analogy type noise predictions.

The success of the acoustic analogy methods in propulsion noise assessment rests upon two elements: (i) a faithful source model; (ii) a robust propagator. The former factor heavily weighs on the statistical properties of turbulent fluctuations (velocity and temperature). In jets, cross-correlation measurements of turbulent velocity components in a flow at various jet operating conditions, and at different locations within the jet exhaust plume, have been examined by a number of investigators – Davies, *et al*.[3], Chu[4], Doty and McLaughlin[5], Bridges and Wernet[6], Wernet[7] , and more recently by Morris and Zaman[8] , among others. These measurements have been invaluable in providing information related to the source correlations of various orders, source convection velocity, time- and length-scales of turbulence, and other parameters of interest in source modeling. Fan exhaust noise would propagate through the external shear layer near the nozzle exit, and could be subject to nearby solid surfaces, most notably a center-body plug. An acoustic analogy approach may be formulated for this noise component provided that equivalent pressure-like sources associated with the fan noise are specified at the nozzle exhaust plane.

Acoustic analogy predictive tools normally use a Reynolds-Averaged Navier-Stokes solver (RANS) for the time-independent nozzle flow calculations. Turbulent velocity components and the dissipation rate of turbulent kinetic energy are among required parameters for source modeling. Examples of such modeling efforts in jets are provided in a number of publications by Tam and Laurent[9], Tam[10] , Morris, *et al.*[11], Leib and Goldstein[12], Leib[13] , Khavaran, *et al.*[14], among others.

Mean flow parameters like velocity and temperature define the propagation Green's Function (GF). In a locally parallel flow the GF would also depend on the axial wave number k_1. An extensive assortment of the GF methods in shear flows, both ducts and jets, is available in the literature that utilize different approximations to reach an analytical solution (see Tam and Auriault[15] , Campos and Kobayashi[16] , Wundrow and Khavaran[17] , Brambley, *et al.*[18] and Gaffney *et al*.[19]).

In a jet exhaust, the dominant value of the axial wave number (here denoted as k_1^*) contributing to the far-field Green's function solution to Rayleigh equation is shown to be a function of the polar observer angle θ, frequency ω, and ambient Mach number M_∞. When the velocity difference between a jet and the ambient is subsonic ($U - U_\infty < c_\infty$), the equation may be solved numerically (exact solution) at this particular wave number, and for the entire range of polar observer angles. The boundary conditions are the initial conditions on the centerline (or the center-body surface), and radiation conditions in the ambient. However, when the velocity difference between the exhaust flow and ambient exceeds the sonic speed, a singularity develops in the governing equation at some source location r_o within the shear layer where factor the $\omega - k_1^* U(r_o)$ vanishes. This singularity also appears in the general form of the GF solution as a second- or a third-order pole, and is different from instability related singularity that occurs at any jet speed when $\omega - k_1 U(r) = 0$.

In section 2 we derive an expression for the GF subject to an impedance-type boundary condition on the center-body plug. Although, ideally, a Wiener-Hopf method is desirable due to inner mixed conditions fore and aft the plug tip, here we formulate the problem subject to a local boundary condition at each stream-wise section. With this assumption, the local inner condition is considered as applicable throughout the jet. In effect, this is similar to the locally parallel mean flow approximation that is imposed on the mean axial velocity and mean density in order to allow an axial Fourier Transform in the usual sense.

Both no-slip and slip conditions on the center-body surface will be discussed. The stationary-phase solution to the propagation equation is presented in section 3 subject to an ambient Mach number $M_\infty < 1$. The radiation angle θ^s at the source is shown to depend on the polar observer angle θ and the ambient Mach number M_∞. Numerical examples (section 4) use analytical representations of the mean velocity and temperature profiles, and present a parametric study of the exact GF solution, applicable to a point source as well as a ring source, as a function of the source location, frequency, flight Mach number, and surface conditions on the center-body. A summary is given in section 5.

2. Green's Function Formulation

Generation and propagation of aerodynamic noise in a transversely sheared mean flow is governed by the third-order wave equation

$$L\pi' = \Gamma, \quad \pi' \cong \frac{p'(\vec{x},t)}{\gamma \bar{p}} \quad . \tag{2.1}$$

In jets source term Γ is the difference between the generalized Reynolds stress components and their Favre-averaged values [1,2] , and for fan noise purposes Γ may be considered as a distribution of pressure-

like sources associated with either broad-band noise or tone noise defined at the engine exhaust plane. The Rayleigh operator L is defined as

$$L \equiv D\left(D^2 - \frac{\partial}{\partial x_j}\left(c^2 \frac{\partial}{\partial x_j}\right)\right) + 2c^2 \frac{\partial U}{\partial x_j}\frac{\partial^2}{\partial x_1 \partial x_j}\ , \quad D \equiv \frac{\partial}{\partial t} + U\frac{\partial}{\partial x_1}\ . \tag{2.2}$$

Upon invoking the locally parallel mean flow approximation, the mean axial velocity U and the speed of sound c are considered as independent of the stream-wise direction x_1, i.e. $U = U(\vec{x}_T), c = c(\vec{x}_T)$, and $\vec{x}_T = (x_2, x_3)$ denotes the span-wise coordinates. The solution to Eq. (2.1) is of the form

$$\pi'(\vec{x}, t) = \int_{\vec{y}} \int_{\tau} G(\vec{x}, t|\vec{y}, \tau)\, \Gamma(\vec{y}, \tau) d\tau d\vec{y}\ , \tag{2.3}$$

where G is the Green's function

$$LG(\vec{x}, t|\vec{y}, \tau) = \delta(\vec{x} - \vec{y})\delta(t - \tau)\ . \tag{2.4}$$

We use the convention that the first two arguments of the GF denote the dependent variables, and the second two are the source variables. In a bounded medium, such as a jet exhaust with a center-body (CB), the above form of solution implies that the GF satisfies certain boundary conditions on the bounding surfaces that would eliminate the surface integrals in the GF formulation.

A Fourier transform (FT) pair with respect to stream-wise coordinate $x_1$and time t is defined as

$$\hat{G}(k_1, \vec{x}_T|\, \vec{y}_T, \omega) = \frac{1}{(2\pi)^2}\int_{-\infty}^{\infty}\int_{-\infty}^{\infty} G(\vec{x}, t|\vec{y}, \tau) e^{-ik_1(x_1 - y_1) + i\omega(t-\tau)}\, d(x_1 - y_1) d(t - \tau), \tag{2.5}$$

with the corresponding inverse FT as

$$G(\vec{x}, t|\vec{y}, \tau) = \int_{-\infty}^{\infty}\int_{-\infty}^{\infty} \hat{G}(k_1, \vec{x}_T|\, \vec{y}_T, \omega) e^{ik_1(x_1 - y_1) - i\omega(t-\tau)}\, dk_1 d\omega. \tag{2.6}$$

Throughout, a circumflex is used to denote a FT variable as defined above. Since the causality condition requires a null solution for $G(\vec{x}, t|\vec{y}, \tau)$ when $t - \tau < 0$, then the integration in the complex ω-plane in Eq. (2.6) should be carried out slightly above the real ω axis (i.e. ω should possess a small positive imaginary component) the avoid the singularities of $\hat{G}(k_1, \vec{x}_T|\, \vec{y}_T, \omega)$ which, as will be seen shortly in Eq. (2.8), occur when $-\omega + k_1 U(\vec{y}_T) = 0$.

Upon applying the above transformation and making appropriate rearrangement, Eq. (2.4) is written as a reduced wave equation

$$(\nabla_T^2 + f(k_1, \vec{x}_T, \omega))\breve{G}(k_1, \vec{x}_T|\, \vec{y}_T, \omega) = \delta(\vec{x}_T - \vec{y}_T), \tag{2.7a}$$

where ∇_T^2 is the Laplacian operator in a span-wise plane. Since Eq. (2.7a) represents a self-adjoint PDE, the newly defined Green's function, $\breve{G}$, is symmetric in variables $\vec{x}_T$ and $\vec{y}_T$

$$\breve{G}(k_1, \vec{x}_T|\, \vec{y}_T, \omega) = \breve{G}(k_1, \vec{y}_T|\vec{x}_T, \omega)\ , \tag{2.7b}$$

and is related to the Green's function of interest $\hat{G}$ as

$$\hat{G}(k_1,\vec{x}_T|\,\vec{y}_T,\omega) = \frac{i}{(2\pi)^2}\frac{1}{c(\vec{x}_T)c(\vec{y}_T)}\frac{-\omega+k_1U(\vec{x}_T)}{\left(-\omega+k_1U(\vec{y}_T)\right)^2}\breve{G}(k_1,\vec{x}_T|\,\vec{y}_T,\omega)\,, \tag{2.8}$$

where

$$f(k_1,\vec{x}_T,\omega) = \kappa_o^2\Phi^2 - k_1^2 - \Phi\nabla_T^2(1/\,\Phi), \tag{2.9}$$

$$\Phi(\vec{x}_T) = \frac{c_\infty}{c(\vec{x}_T)}\left(-1+\frac{k_1}{\kappa_o}M(\vec{x}_T)\right), \qquad M(\vec{x}_T) = \frac{U(\vec{x}_T)}{c_\infty}, \qquad \kappa_o = \frac{\omega}{c_\infty} \tag{2.10}$$

In axisymmetric jets, polar coordinates (r,ϕ) are used in place of $\vec{x}_T$, thus

$$\begin{aligned} f(k_1,r,\omega) &= \chi^2 - \mathbb{C}^2 - 2\frac{(k_1M')^2}{(-\kappa_o+k_1M)^2} + \frac{k_1}{-\kappa_o+k_1M}\left(M'' + \frac{c^{2\prime}}{c^2}M' + \frac{1}{r}M'\right), \\ \chi^2 &= \left(\frac{c_\infty}{c}(-\kappa_o+k_1M)\right)^2 - k_1^2, \\ \mathbb{C}^2 &= \frac{1}{2}\frac{\partial}{\partial r}\left(\frac{c^{2\prime}}{c^2}\right) + \frac{1}{4}\left(\frac{c^{2\prime}}{c^2}\right)^2 + \frac{1}{2r}\frac{c^{2\prime}}{c^2}. \end{aligned} \tag{2.11}$$

where prime notation on the mean flow variables $M(r)$ and $c^2(r)$ signifies a radial differentiation. Using a similar notation $\vec{y}_T \equiv (r_o,\phi_o)$ to identify source location, the GF $\breve{G}$ is written as a summation of circumferential modes in polar coordinates

$$\breve{G}(k_1,\vec{x}_T|\,\vec{y}_T,\omega) = \sum_{n=-\infty}^{+\infty}\breve{G}_n(k_1,r|r_o,\omega)\,e^{in(\phi-\phi_o)}. \tag{2.12}$$

The delta function on the RHS of Eq. (2.7a) may be replaced with $\delta(\vec{x}_T-\vec{y}_T) = \delta(r-r_o)\delta(\phi-\phi_o)/r$, and upon using the identity

$$\delta(\phi-\phi_o) = \frac{1}{2\pi}\sum_{n=-\infty}^{+\infty}e^{in(\phi-\phi_o)}\,, \tag{2.13}$$

equation (2.7a) is written for each mode component

$$\left(\frac{d^2}{dr^2} + \frac{1}{r}\frac{d}{dr} + f(k_1,r,\omega) - \frac{n^2}{r^2}\right)\breve{G}_n(k_1,r|r_o,\omega) = \frac{1}{2\pi r}\delta(r-r_o), \quad n=-\infty,\cdots,+\infty \tag{2.14}$$

We seek a solution to equation (2.14) applicable to a far field observer $(r\to\infty)$, and with the source located in the interval $r_1 \le r_o \le r_2$. In exhaust nozzles that are devoid of an external center-body, radius r_1 is at the centerline, however when a plug is present (figure 1) appropriate boundary conditions need to be implemented on its surface at $r_1 = r_s$ that would eliminate surface integrals in the GF formulation. Radius r_2 is referred to as the outer exhaust boundary where the mean flow gradients approach zero. Subsequently, at $r > r_2$ propulsion-related noise sources are absent, and the mean velocity and the sound speed

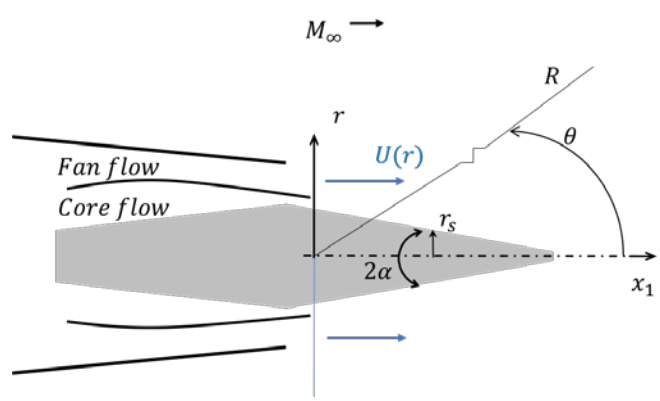

Figure 1. Jet exhaust with a center-body.

reach their respective ambient values of U_∞ and c_∞ where an exterior solution may readily be written down

$$\left(\frac{d^2}{dr^2} + \frac{1}{r}\frac{d}{dr} + \chi_\infty^2 - \frac{n^2}{r^2}\right)\breve{G}_n(k_1, r|r_o, \omega) = 0, \quad r > r_2 \tag{2.15a}$$

and

$$\chi_\infty^2 = (-\kappa_o + k_1 M_\infty)^2 - k_1^2, \quad M_\infty = U_\infty / c_\infty. \tag{2.15b}$$

Mach number M_∞accounts for the flight effect. When $\chi_\infty^2 > 0$, the exterior solution is of the form of a Hankel function

$$\breve{G}_n(k_1, r|r_o, \omega) = b_n(k_1, \omega) H_n^{(1)}(r\chi_\infty). \quad r > r_2 \tag{2.15c}$$

Dimensionless parameter $b_n(k_1, \omega)$ denotes the solution coefficient, and parameter χ_∞ is the positive root of χ_∞^2 for an outgoing wave. It will be shown later that χ_∞^2 remains positive for the dominant value of wave-number component k_1 as long as $M_\infty < 1$. For negative values of χ_∞^2 the branch-cut should be selected as $\chi_\infty = +i\sqrt{|\chi_\infty^2|}$ to obtain an exponentially decaying (evanescent) wave. These latter waves do not radiate to the far field, however their interaction with the nearby structural components like aircraft wings, flaps, pylon, etc. may result in low-frequency jet surface interaction noise [20,21,22].

The boundary conditions on the CB are obtained from the linearized momentum equation. Upon writing the fluid velocity components as the sum of Favre-averaged and fluctuating components, where $v_i = \widetilde{v}_i + v_i'$ $(i = 1,2,3)$, and using the locally parallel mean flow approximation, $\widetilde{\boldsymbol{v}} = U(r)\,\vec{\imath}$, we apply a no-slip condition on the base flow at the surface $(U = 0, r \to r_s)$

$$\frac{\partial(\rho v_i')}{\partial t} + \frac{\partial p'}{\partial x_i} = 0, \quad r = r_s. \tag{2.16}$$

For now, let's consider the external plug as a conical geometry with angle α (figure 1), and apply FT to variables t and x_1 in Eq. (2.16). The axial and radial components of the transformed momentum equation are

$$-i\omega\rho\,\hat{v}_1' + ik_1\,\hat{p}' = 0, \tag{2.17a}$$

$$-i\omega\rho\,\hat{v}_r' + \frac{\partial}{\partial r}\,\hat{p}' = 0. \tag{2.17b}$$

where ρ is the mean density. For a locally reactive boundary, the normal component of velocity fluctuations $v_\perp' = v_1' \sin\alpha + v_r' \cos\alpha$ (with the normal directed into the fluid) is related to the pressure fluctuations on the CB through surface impedance function $Z(\omega)$

$$\hat{p}' = -Z(\omega)\,\hat{v}_\perp'. \quad (on\ the\ surface) \tag{2.17c}$$

Equations (2.17a), (2.17b), and (2.17c) are combined to show

$$-i\left(k_1 \sin\alpha + \frac{\omega\rho}{Z(\omega)}\right)\hat{p}' = \cos\alpha\,\frac{\partial\,\hat{p}'}{\partial r}. \qquad (on\ the\ surface) \tag{2.18}$$

Equation (A5) in appendix A describes the corresponding boundary condition when a slip velocity is imposed on the CB surface.

Since the FT of a convolution is the product of Fourier transforms, Eq. (2.3) implies

$$\hat{\pi}'(k_1, \vec{x}_T, \omega) = (2\pi)^2 \int_{\vec{y}_T} \hat{G}(k_1, \vec{x}_T | \vec{y}_T, \omega)\, \hat{\Gamma}(k_1, \vec{y}_T, \omega) d\vec{y}_T, \tag{2.19}$$

and when used in Eq. (2.18) we arrive at

$$-i\left(k_1 \sin\alpha + \frac{\omega\rho}{Z(\omega)}\right) \hat{G}(k_1, \vec{x}_T | \vec{y}_T, \omega) = \frac{\partial}{\partial r} \hat{G}(k_1, \vec{x}_T | \vec{y}_T, \omega) \cos\alpha\,. \quad (on\ the\ surface) \tag{2.20}$$

Equations (2.8) and (2.12) are substituted in (2.20) to show the surface boundary condition applicable to $\breve{G}_n(k_1, r|r_s, \omega)$

$$\frac{\partial}{\partial r} \breve{G}_n(k_1, r|r_o, \omega) - \psi \breve{G}_n = 0, \quad r = r_s \tag{2.21a}$$

$$\psi(k_1, r, \omega, \bar{Z}) = \frac{-i}{\cos\alpha}\left(k_1 \sin\alpha + \frac{\kappa_o}{\bar{Z}} \frac{c_\infty^2}{c^2}\right) + \frac{c^{2\prime}}{2c^2} + \frac{k_1}{\kappa_o} M'(r), \tag{2.21b}$$

where $\bar{Z}(\omega) = Z(\omega)/\rho_\infty c_\infty$ denotes the normalized surface impedance, and the usual assumption of constant static pressure $\gamma\bar{p} = \rho c^2 = constant$ is employed in the above derivations. Appendix B shows that condition (2.21a) eliminates the surface integrals in the GF formulation of the acoustic field.

The solution to the second-order linear differential equation (2.14) may be expressed in terms of two linearly independent solutions $V_n^{(j)}(k_1, r, \omega)$ to the homogeneous equation

$$\left(\frac{d^2}{dr^2} + \frac{1}{r}\frac{d}{dr} + f(k_1, r, \omega) - \frac{n^2}{r^2}\right) V_n^{(j)}(k_1, r, \omega) = 0, \quad j = 1,2 \tag{2.22}$$

For brevity, variables k_1 and ω are kept out of the argument of $V_n^{(j)}$ in writing the solution. Since the interest is primarily in the far field, only the $r > r_o$ form of the solution is discussed

$$\breve{G}_n(k_1, r|r_o, \omega) = \frac{1}{2\pi r_o} \frac{V_n^{(2)}(r) V_n^{(1)}(r_o)}{W\left(V_n^{(1)}, V_n^{(2)}\right)_{r=r_o}}\,, \qquad r > r_o \tag{2.23a}$$

where W is the Wronskian

$$W\left(V_n^{(1)}, V_n^{(2)}\right) = V_n^{(1)} \frac{dV_n^{(2)}}{dr} - V_n^{(2)} \frac{dV_n^{(1)}}{dr}\,. \tag{2.23b}$$

In view of Eq. (2.23a) the initial amplitudes should not have a bearing on the GF solution, subsequently $V_n^{(1)}$ and $V_n^{(2)}$ are normalized at the starting point – thus the boundary conditions are expressed as

$$\begin{cases} V_n^{(1)}(r) = V_n^{(2)}(r) = 1, & r = r_s \\ \frac{\partial}{\partial r} V_n^{(1)}(r) - \psi V_n^{(1)}(r) = 0, & r = r_s \\ V_n^{(2)}(r) = b_n(k_1, \omega) H_n^{(1)}(r\chi_\infty), & r \geq r_2 \end{cases} \tag{2.24}$$

Upon substituting Eq. (2.23a) into (2.12), and next into (2.8), we apply an inverse FT to $\hat{G}(k_1, \vec{x}_T | \vec{y}_T, \omega)$ to obtain the frequency-domain GF

$$G(\vec{x},\vec{y};\omega) = \frac{i}{(2\pi)^3}\frac{1}{c(r)\,c(r_o)}\sum_{n=0}^{\infty}\varepsilon_n \cos(n\,\phi)$$
$$\times \int_{-\infty}^{\infty}\frac{-\omega+k_1U(r)}{\left(-\omega+k_1U(r_o)\right)^2}\frac{V_n^{(2)}(k_1,r,\omega)V_n^{(1)}(k_1,r_o,\omega)}{rW\left(V_n^{(1)},V_n^{(2)}\right)}e^{ik_1(x_1-y_1)}dk_1 \tag{2.25}$$

where $\varepsilon_0 = 1, \varepsilon_n = 2$ for $n \geq 1$, and angle ϕ (also denoted as $\Delta\phi$) is used as the azimuthal separation between the source and the observer.

3. Far-field Acoustics

Since the interest lies in the far-field noise, we use the asymptotic form of the Hankel function to write $V_n^{(2)}$ as

$$V_n^{(2)}(k_1,r,\omega) \sim b_n(k_1,\omega)\sqrt{\frac{2}{\pi\, r\chi_\infty}}\,e^{i\left(r\chi_\infty-\frac{n\pi}{2}-\frac{\pi}{4}\right)}. \qquad r\to\infty \tag{3.1}$$

Equation (2.25) is now expressed as

$$G(\vec{x},\vec{y};\omega) = \frac{i}{(2\pi)^3}\frac{1}{c(r)\,c(r_o)}\sqrt{\frac{2}{\pi r}}\sum_{n=0}^{\infty}\varepsilon_n\cos(n\,\phi)Q_n(r|r_o,\omega)e^{-i\left(\frac{n\pi}{2}+\frac{\pi}{4}\right)}, \tag{3.2}$$

$$Q_n(r|r_o,\omega) = \int_{-\infty}^{\infty}\frac{-\omega+k_1U(r)}{\left(-\omega+k_1U(r_o)\right)^2}V_n^{(1)}(k_1,r_o,\omega)\Lambda(V_n^{(1)},H_n^{(1)})\frac{1}{\sqrt{\chi_\infty}}e^{ir\Theta}dk_1, \tag{3.3}$$

$$\Theta(k_1,\omega,M_\infty) = (\,k_1/\tan\theta+\chi_\infty\,), \qquad r\to\infty \tag{3.4}$$

where (R,θ) are spherical polar coordinates with angle θ measured from the downstream axis (figure 1), $R = |\vec{x}-\vec{y}|$, $r = R\sin\theta$, and Θ in the exponent represents a real function. Factor $\Lambda = \frac{b_n(k_1,\omega)}{rW\left(V_n^{(1)},V_n^{(2)}\right)}$ in Eq. (3.3) depends on parameters k_1 and ω only. And since the product $rW\left(V_n^{(1)},V_n^{(2)}\right)$ is independent of r, the radial distance may be pushed to $r \geq r_2$ where the mean flow gradients are absent and solution $V_n^{(2)}$ takes the familiar form of a Hankel function $b_n(k_1,\omega)H_n^{(1)}(r\chi_\infty)$, subsequently coefficient $b_n(k_1,\omega)$ is eliminated from this ratio

$$\Lambda(V_n^{(1)},H_n^{(1)}) = \frac{\frac{1}{r}}{V_n^{(1)}(k_1,r,\omega)\frac{\partial H_n^{(1)}(r\,\chi_\infty)}{\partial r} - \frac{\partial V_n^{(1)}(k_1,r,\omega)}{\partial r}H_n^{(1)}(r\,\chi_\infty)}, \quad r\geq r_2 \tag{3.5}$$

The integral in Eq. (3.3) may now be evaluated using the stationary phase technique when $\kappa_o R \gg 1$, i.e. when the wavelength is small compared to the distance from source to the observer. The point of stationary phase is designated with superscript "*"

$$Q_n(r|r_o,\omega) \sim \sqrt{\frac{2\pi}{r}}\,\frac{\sqrt{\mathrm{P}}}{c_\infty\kappa_o}\frac{-1+M(r)\cos\theta^s}{(1-M(r_o)\cos\theta^s)^2}V_n^{(1)}(k_1^*,r_o,\omega)\Lambda(V_n^{(1)},H_n^{(1)})\Big|_{k_1=k_1^*}e^{ir\Theta(k_1^*,\omega,M_\infty)-\frac{i\pi}{4}}, \tag{3.6}$$

where

$$\frac{k_1^*}{\kappa_o} = \cos\theta^s = \frac{1}{1-M_\infty^2}\left(-M_\infty + \frac{\cos\theta}{\sqrt{1-M_\infty^2\sin^2\theta}}\right), \tag{3.7}$$

$$\mathrm{P} = \sin^2\theta \,/\, (1 - M_\infty^2 \sin^2\theta), \tag{3.8}$$

$$\Theta(k_1^*, \omega, M_\infty) = \kappa_o \Psi / \sin\theta\,, \;\; \Psi = \frac{1}{(1-M_\infty^2)}\left(-M_\infty\cos\theta + \sqrt{1 - M_\infty^2\sin^2\theta}\;\right). \tag{3.9}$$

We require a subsonic ambient Mach number, $M_\infty < 1$, therefore parameter P in Eq. (3.8) remains positive, and the positive root of factor $\sqrt{\mathrm{P}}$ should be placed in Eq. (3.6). This condition also assures radiation requirement $\chi_\infty^* = \chi_\infty(k_1^*, \omega) = \kappa_o\sqrt{\mathrm{P}} > 0$. Using these results in Eq. (3.2), we arrive at the frequency-domain Green's function solution to Eq. (2.4)

$$G(\vec{x}, \vec{y}; \omega) \sim \frac{-1}{4\pi^3}\frac{1}{c_\infty^2\, c(r_o)}\frac{e^{i\kappa_o R\Psi}}{\kappa_o R}\frac{(1 - M_\infty\cos\theta^s)}{(1 - M(r_o)\cos\theta^s)^2}\frac{1}{\sqrt{1 - M_\infty^2\sin^2\theta}}$$

$$\times \sum_{n=0}^{\infty} \varepsilon_n e^{-i\frac{n\pi}{2}} \cos(n\,\phi)\, V_n^{(1)}(k_1^*, r_o, \omega)\Lambda(V_n^{(1)}, H_n^{(1)})\Big|_{k_1 = k_1^*} \tag{3.10}$$

and

$$G(\vec{x}, t|\vec{y}, \tau) = \int_{-\infty}^{\infty} G(\vec{x}, \vec{y}; \omega) e^{-i\omega(t-\tau)} d\omega. \tag{3.11}$$

The GF expression (Eq. 3.10) depends on the solution $V_n^{(1)}(k_1^*, r, \omega)$ of the second-order ODE (Eq. 2.22) and the far-field behavior of the exterior solution $V_n^{(2)}(k_1^*, r_2, \omega)$. The latter quantity is of course a known function as described above. The remaining challenge is solution $V_n^{(1)}$, which is best obtained numerically, and subject to the two initial conditions stated in Eq. (2.24).

In acoustic analogy type noise simulations, the mean flow information required in solving Eq. (2.22) comes from a RANS flow solver. Suitable high-order interpolation will be required to obtain function $f(k_1, r, \omega)$ as defined in Eq. (2.11). In absence of a CB, the initial conditions on the centerline should replace Eq. (2.24). Here the solution behaves like $V_n^{(1)} \to r^n$ as $r \to 0$, thus the two conditions are simplified as

$$\begin{cases} V_n^{(1)}(k_1^*, r, \omega) = \epsilon\,, \\ \frac{\partial}{\partial r} V_n^{(1)}(k_1^*, r, \omega) \;= n, \end{cases} \qquad r = \epsilon, \quad n \geq 1 \tag{3.12}$$

for an arbitrary small number $\epsilon \to 0$. When $n = 0$ the centerline conditions are $V_n^{(1)}(k_1^*, r, \omega) = 1$, and $\frac{\partial}{\partial r} V_n^{(1)} = 0$.

Appendix C shows that Eq. (2.22) may be written in a form more suitable for numerical discretization. This form of the differential equation, commonly referred to as the Pridmore-Brown (PB) equation[23] would only require the first-order derivatives of the mean flow variables. The GF solution to the PB equation and the related initial conditions on the CB surface are detailed in Appendix C. Numerous

applications of the PB equation in connection with the boundary layer and duct noise are available in the literature [16,19,24].

Before proceeding with the GF computations, it is worthwhile to examine the relation between the radiation angle θ^s and the observer angle θ as stated in Eq. (3.7). This is shown in figure 2 using the ambient Mach number M_∞ as a parameter. It appears as if only under static condition $M_\infty = 0$ could a source radiate to the upstream angle $\theta = \pi$. Flight effect seems to limit the maximum upstream reach in angle θ as seen from the intersect point of each parametric curve with line $\theta^s = \pi$. This maximum angle, indicated as θ_{Max}, is shown more markedly in figure 3 by letting $\cos\theta^s = -1$ in Eq. (3.7) and solving for angle θ as a function of M_∞. When $\theta > \theta_{Max}$ at a selective ambient Mach number, the right-hand side of Eq. (3.7) would descend below -1, thus θ^s would become a complex number.

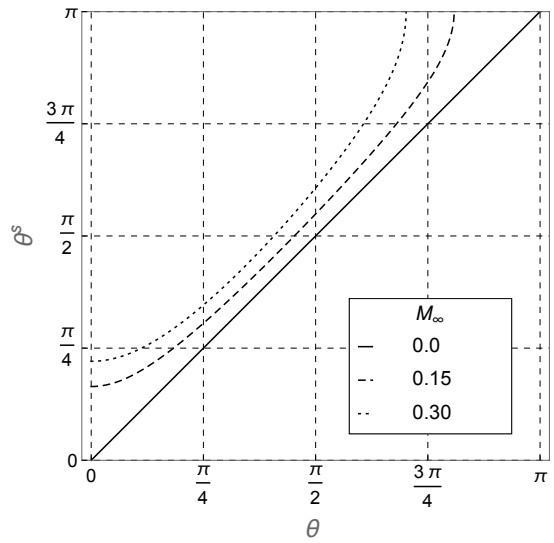

Figure 2. Radiation angle vs. observer angle in flight.

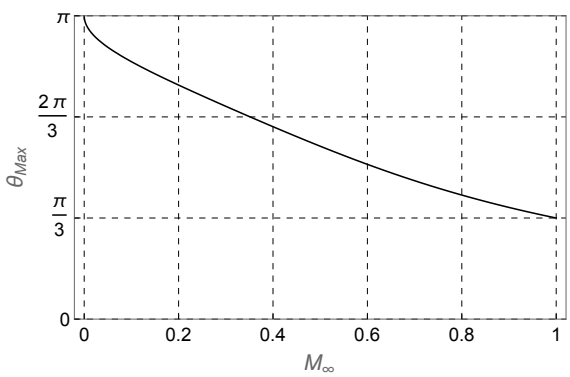

Figure 3. Maximum reach of observer angle θ in flight for real values of radiation angle θ^s.

Physically speaking, the only real parameters of interest in the analysis are the observer angle θ and the wave number ($k_1 = k_1^*$) – both remain as real numbers even when θ^s is a complex number. However, the magnitude of k_1 would now be larger than κ_o, which is clearly a counterintuitive outcome. The required radiation condition $\chi_\infty^2(k_1^*, \omega) > 0$, which can alternatively be phrased as $k_1^* < \kappa_o/(1 + M_\infty)$, still holds even when $\theta > \theta_{Max}$. Simply stated, θ^s is now an analytic continuation of $\arccos\theta^s$.

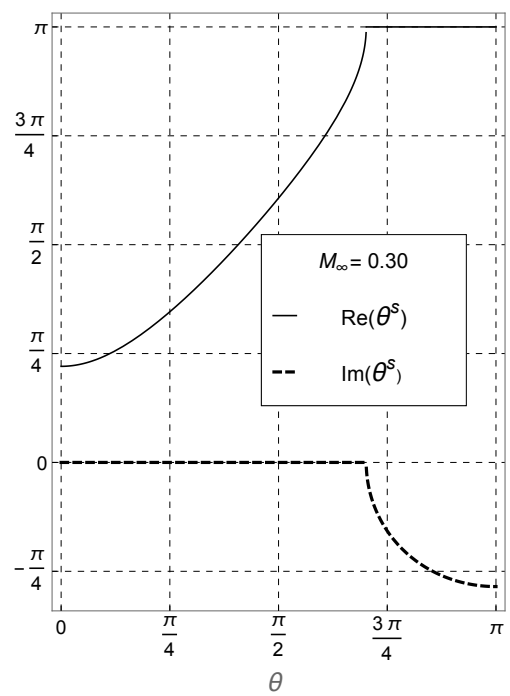

Figure 4. Complex radiation angle in flight at $M_\infty = 0.30$.

An illustration of complex radiation angle θ^s vs. θ at Mach number $M_\infty = 0.30$ is shown in figure 4. While the real component of θ^s remains as π, it acquires a negative imaginary component for all $\theta > 126.30^o$ at this particular value of M_∞. Green's function computations beyond θ_{Max} will be demonstrated in the next section.

4. Numerical Results

Computations presented here use analytical representations of the mean flow velocity and temperature profiles. Parameters of interest are the exhaust Mach number $M_j = \frac{U_j}{c_j}$, liner-impedance function $\bar{Z}(\omega)$ on the CB surface, the ambient Mach number M_∞, and stagnation temperature ratio $T_R = \frac{T^o}{T_\infty}$, where T^o denotes the upstream plenum stagnation temperature. Distances are normalized as $\eta \equiv r/D$ where D is a nominal jet diameter. Computational results are shown for a normalized Green's function G_N defined as

$$G_N(\vec{x},\vec{y};\omega) \equiv G(\vec{x},\vec{y};\omega)/\left(\frac{1}{\pi^2 c_\infty^3}\frac{e^{i\kappa_o R\Psi}}{4\pi R/D}\right), \tag{4.1}$$

and at selective values of the Strouhal frequency $St = \frac{\omega D}{2\pi\, U_j}$. Wave number κ_o is evaluated as

$$\kappa_o D = 2\pi\, St\, \frac{U_j}{c_\infty}, \quad \frac{U_j}{c_\infty} = M_j\left(\frac{T_j}{T_\infty}\right)^{1/2}, \quad \frac{T_j}{T_\infty} = \frac{T_R}{1+\frac{\gamma-1}{2}M_j^2} \tag{4.2}$$

where γ is the ratio of the specific heats.

4.1 Flow Over the Center-Body

In practical applications, numerically calculated flow profiles subject to the appropriate upstream conditions for the core and bypass streams should be imported from a RANS solver for GF calculations. Here we use Hyperbolic functions to simulate a mean velocity profile compatible with the similarity rules of Tennekes and Lumley[25] in a parallel base flow

$$\frac{U(\eta)}{U_j} = \begin{cases} 1 - d_o\,\mathrm{sech}\left(\frac{\eta-\eta_s}{d_1}\right), & \eta_s \le \eta < 2\eta_s + \delta_w \\ \frac{1}{2}\left(1+\frac{U_\infty}{U_j}\right) - \frac{1}{2}\left(1-\frac{U_\infty}{U_j}\right)\tanh\big(d_2(\eta-0.5)\big). & \eta \ge 2\eta_s + \delta_w \end{cases} \tag{4.3}$$

Parameter $\eta_s = r_s/D$ signifies the normalized local radius at the CB surface, and δ_w denotes the wall boundary layer (BL) thickness, i.e. the radial distance from the CB surface at which the mean velocity is $0.99U_j$.

Parameter $d_o = 1$ in Eq. (4.3) will be reduced to a positive number smaller than one later on (section 4.2) to simulate the velocity deficit near the centerline at a stream-wise location aft the CB plug tip $(\eta_s = 0)$. Parameter d_1 determines the BL thickness as per $\delta_w = 5.298d_1$, and d_2 determines the external decay of the profile – increasing d_2 would yield a top-hat profile typical of the near-exit flow, while decreasing d_2 would represent a fully developed profile further downstream. The mean velocity profile U/c_∞ is shown in figure 5 using parameters $(M_\infty = 0.30, M_j = 0.90, T_R = 2.0)$ that yield an exhaust acoustic Mach number of $M_a = U_j/c_\infty = 1.18$. The remaining parameters are selected as $\eta_s = 0.10$, and $(d_1, d_2) = (1.0\times10^{-2},\ 32.0)$. The mean static temperature is modeled as a composite of two profiles – the first profile is obtained by placing $U(\eta)$ into Crocco-Busemann law, presently modified to account for the ambient Mach number

$$\frac{T_1(\eta)}{T_j} = -C_1\left(\frac{\frac{U}{U_j}-\frac{U_\infty}{U_j}}{1-\frac{U_\infty}{U_j}}\right)^2 + C_3\left(\frac{\frac{U}{U_j}-\frac{U_\infty}{U_j}}{1-\frac{U_\infty}{U_j}}\right) + C_2\,, \quad \frac{T_1(\eta)}{T_\infty} = \frac{1}{C_2}\frac{T_1(\eta)}{T_j} \tag{4.4}$$

$$C_1 = \frac{\gamma-1}{2}M_j^2,\ \ C_2 = \frac{1}{T_R}(1+C_1),\ \ C_3 = 1 + C_1 - C_2.$$

To circumvent a descent of the near-surface temperature below the ambient temperature, as would be predicted by Eq. (4.4), we introduce a second profile $T_2(\eta)$ near the CB surface

$$\frac{T_2(\eta)}{T_\infty} = \frac{1}{2} - \frac{1}{2}\tanh\big(d_3(\eta - d_4)\big). \tag{4.5}$$

Using $(d_3, d_4) = (50,\ 0.095)$ a composite temperature profile $T(\eta) = T_1(\eta)$ $+T_2(\eta)$ and the corresponding sound speed $c = \sqrt{\gamma \Re T}$ are shown in figure 5.

In carrying out the GF computations, we first observe that identical results are obtained by solving either Eq. (3.10) or the PB equation (see Eq. C6, Appendix C). For this purpose, predictions are presented at a single mode number $(n = 1)$, and at $(St = 1, \theta = \pi/3, \Delta\phi = 0)$.

Figure 6 shows G_N as evaluated from Eq. (3.10) using a rigid CB $(\bar{Z} \to \infty)$ with cone angle $\alpha = \pi/6$. Similar computations were carried out with the PB equation (Eqs. C6 and C7 Appendix C). The ratio of the two results at an arbitrary mode number n

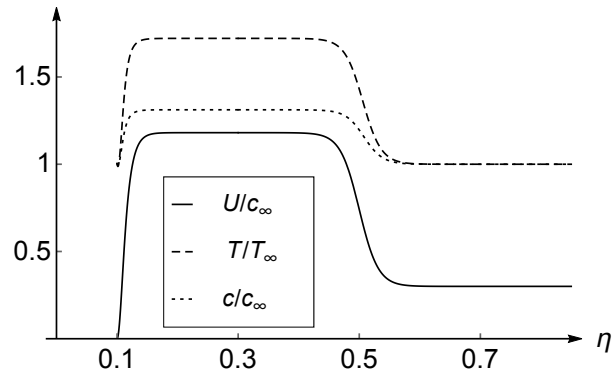

Figure 5. Mean flow profiles: axial velocity (solid line); static temperature (dashed line), and sound speed (dotted line), with $M_j = 0.90, T_R = 2, M_\infty = 0.30, \eta_s = 0.10$.

$$\frac{G_{N,1}}{G_{N,2}} \equiv \left(\frac{c_\infty}{c(r_o)}\ \frac{1-M(r_o)\cos\theta^s}{1-M_\infty\cos\theta^s}\ \frac{V_n^{(1)}(k_1^*, r_o, \omega)}{g_n^{(1)}(k_1^*, r_o, \omega)}\right)\frac{\Lambda(V_n^{(1)}, H_n^{(1)})}{\Lambda(g_n^{(1)}, H_n^{(1)})}\Bigg|_{k_1 = k_1^*}, \tag{4.6}$$

should be equal to 1.0 independent of source location r_o. This is corroborated in figure 7 at mode $n = 1$ within the source interval $\eta_s \le \eta \le 1.5$, and can similarly be repeated for other modes.

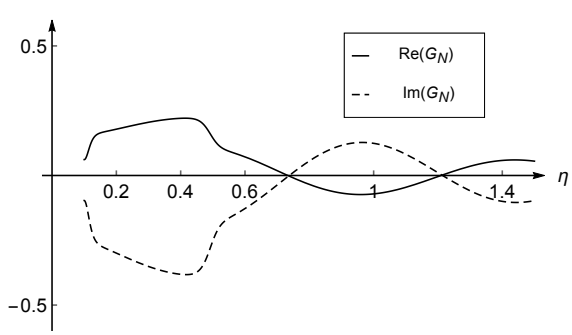

Figure 6. Green's function G_N at a selective single mode n = 1 and at (St = 1.0, $\theta = \pi/3, \Delta\phi = 0$) – using flow definitions of figure 5 with a rigid center- body ($\alpha = \pi/6$).

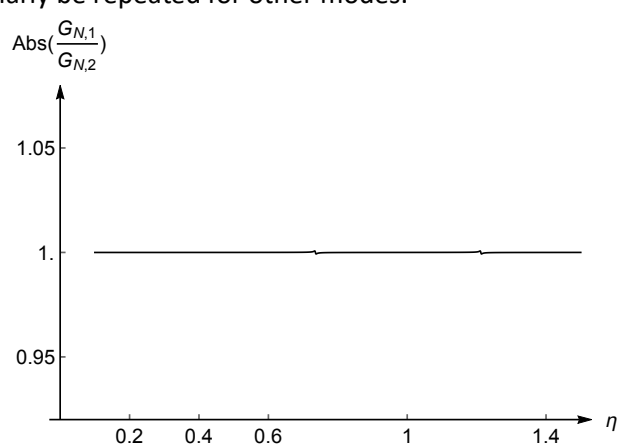

Figure 7. Ratio of the two Green's functions (Eq. 4.6) at a selective mode number n = 1.

The effect of surface treatment on the GF is examined in figure 8 at a complex impedance $\bar{Z} = (0.25, 0.25)$ while the remaining parameters remain the same as in figure 6. Contrasting figure 6 with 8, it is observed that asides from changes in the overall shape (and a reduction in the GF magnitude within the source region), the zero intersects for the real and imaginary components of the GF are now out of phase.

In the next step, summation over sufficient mode numbers is carried out to reach a converged solution. The required modes would increase in number at higher frequencies. Shown in figure 9 is the GF, G_N, corresponding to a rigid surface using a local CB radius $\eta_s = 0.10$, polar angle $\theta = 60^o$, and with source/observer azimuthal separation $\Delta\phi = 0$. The real and imaginary components and the magnitude of the GF are shown subject to the flow profiles in figure 5.

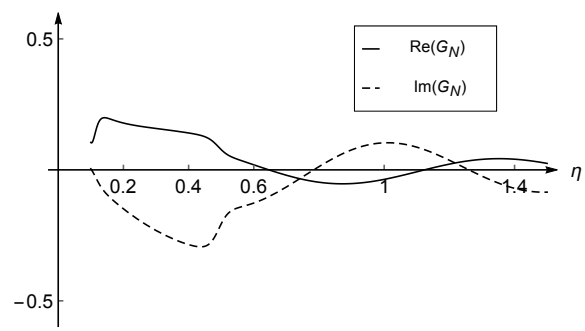

Figure 8. Same as figure 6, but using a lined center-body with surface impedance $\bar{Z} = (0.25, 0.25)$.

Similar displays of the GF are provided for a lined CB with surface impedance function $\bar{Z} = (0.50, 0.50)$ in figure 10, and for an exhaust without a CB in figure 11. The mean flow in the latter case uses a top-hat velocity profile defined by the hyperbolic tangent function in Eq. (4.3) valid for $(\eta \geq 0)$. The corresponding static temperature is defined according to function $T_1(\eta)$ in Eq. (4.4).

Further, the significance of the source/observer azimuthal separation at $\Delta\phi = \pi$ is shown in figures 12, 13 and 14 using the same conditions as those in figures 9, 10, and 11, respectively. Generally speaking, a reduction in the magnitude of the GF is noticed with increasing $\Delta\phi$. Figures 9 through 14 use a series summation of 20 modes for a converged GF.

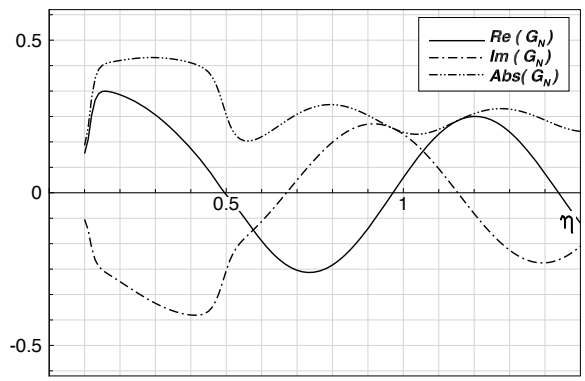

Figure 9. Green's function G_N $(St = 1.0, \theta = 60^o, \Delta\phi = 0)$ at flow definitions of figure 5 $(M_j = 0.90, T_R = 2, M_\infty = 0.30)$, and a rigid center-body at radius $(\eta_s = 0.10)$.

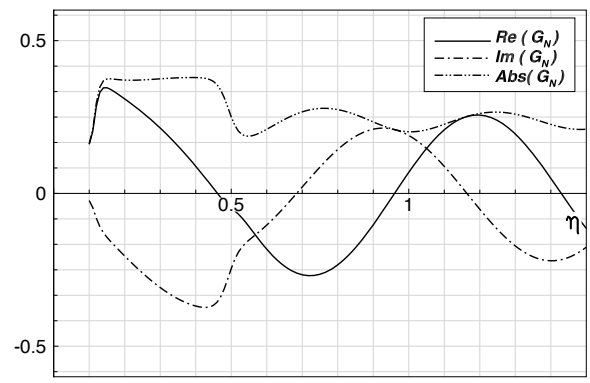

Figure 10. As in figure 9, but with a lined center-body $\overline{Z} = (0.50, 0.50)$.

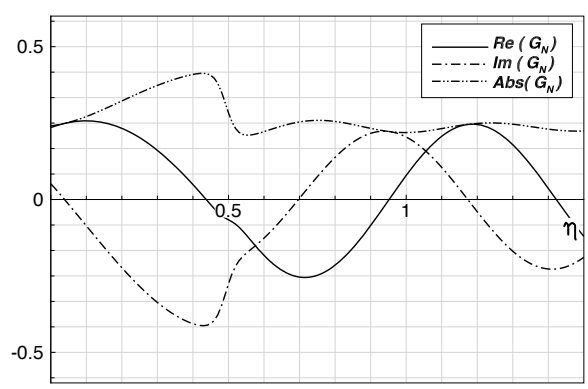

Figure 11. As in figure 9, but without a center-body.

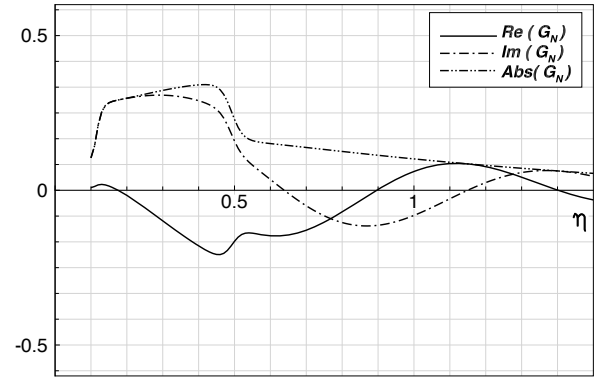

Figure 12. Green's function G_N $(St = 1.0, \theta = 60^o, \Delta\phi = \pi)$ at flow definitions of figure 5 $(M_j = 0.90, T_R = 2, M_\infty = 0.30)$, and a rigid center-body at radius $(\eta_s = 0.10)$.

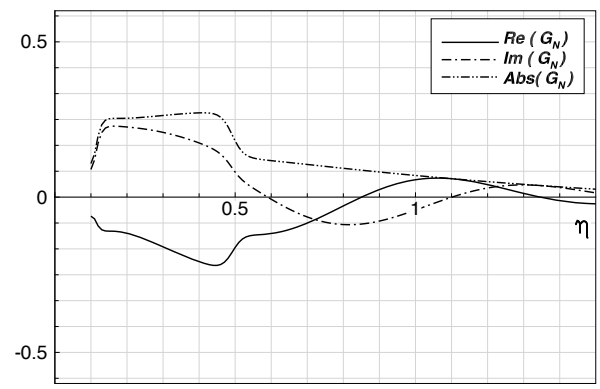

Figure 13. As in figure 12, but with a lined center-body $\overline{Z} = (0.50, 0.50)$.

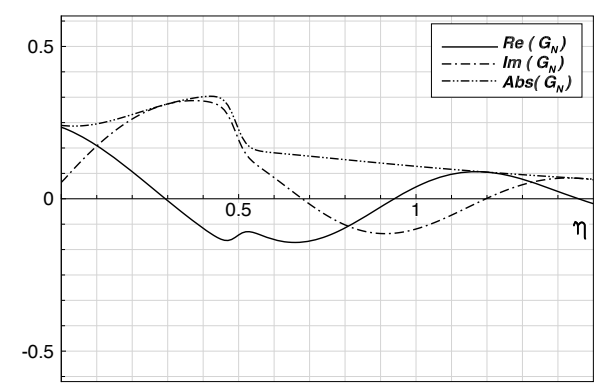

Figure 14. As in figure 12, but in absence of a center-body.

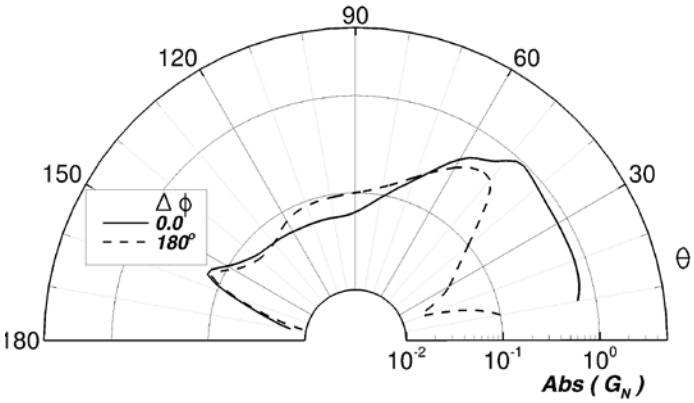

Figure 15. Point source directivity ($St = 1.0, \eta_o = 0.40$) at flow definitions of figure 5 ($M_j = 0.90, T_R = 2, M_\infty = 0.30$) with a rigid center-body: $\Delta\phi = 0$ (solid- line); $\Delta\phi = 180^o$ (dashed-line).

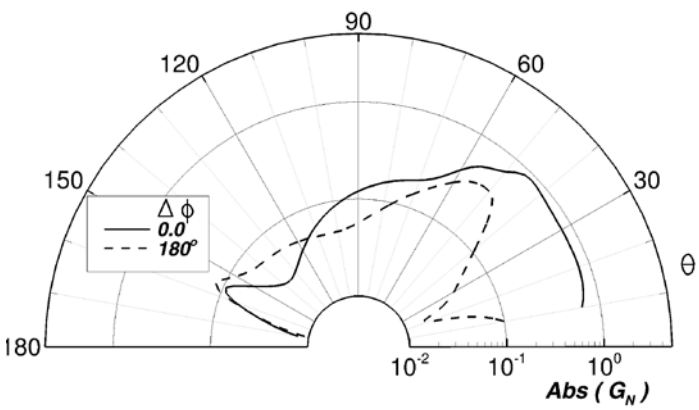

Figure 16. As in figure 15, but with a lined center-body $\bar{Z} = (0.50, 0.50)$.

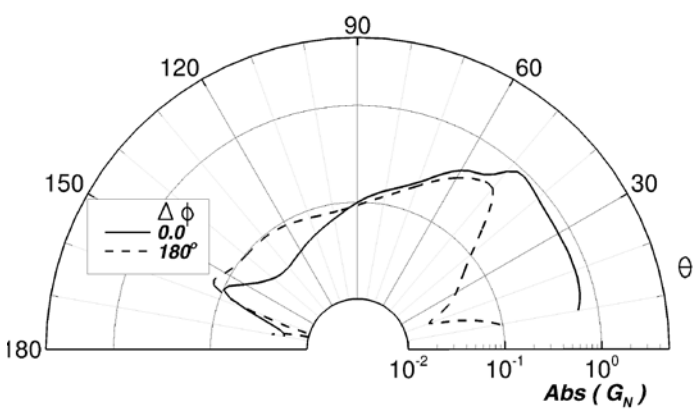

Figure 17. As in figure 15, but in absence of a center-body.

Next, we examine the GF at a selective source location, but for a range of polar observer angles θ, while source/observer azimuthal separation $\Delta\phi$ is used as a parameter. Figures 15 to 17 show the polar directivity of a point source at $\eta_o = 0.40$ and $St = 1.0$ using the flow definitions of figure 5. Directivity plots are shown using a rigid boundary in figure 15, a lined CB with $\bar{Z} = (0.50, 0.50)$ in figures 16, and an exhaust without a CB (figure 17). It is seen that with $\Delta\phi = 0$, the corresponding GF dominates at aft angles ($\theta < \pi/2$), whereas the GF associated with $\Delta\phi = \pi$ dominates the former at forward angles ($\theta > \pi/2$). The effect of the surface liner on the GF is best described in terms of a ring source directivity as will be seen shortly. It is noted that these computations were carried out to an upstream polar angle of $\theta = 170^o$, well beyond transitions point of $\theta = 126.30^o$ at which the radiation angle θ^s becomes a complex number at $M_\infty = 0.30$ (see complex radiation angles in figure 4). When angle θ^s is complex, factor $\cos\theta^s$ may be replaced with $(-\cosh\theta_i^s)$.

In axisymmetric jets, a ring source directivity factor is defined by integrating the product of the GF and its conjugate with respect to the source angle

$$D(r_o, \theta) \equiv \int_0^{2\pi} G_N G_N^* \, d\phi_o. \tag{4.7}$$

The above directivity factor is commonly used in carrying out the source/GF volume integration in acoustic analogy-type noise predictions assuming that the elementary source correlation volumes are azimuthally uniform and compact. Goldstein & Leib[26] examine the effect of source azimuthal non-compactness by coupling various source Fourier components only with their respective propagator modes.

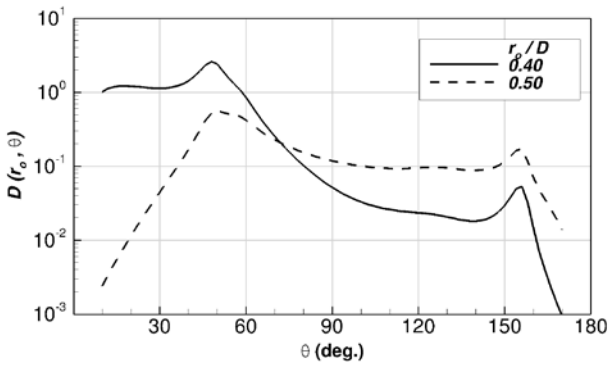

Figure 18. Ring source directivity ($St = 1.0$) at flow definitions of figure 5 with a rigid center-body, and ring sources of radii: $\eta_o = 0.40$ (solid- line); $\eta_o = 0.50$ (dashed-line).

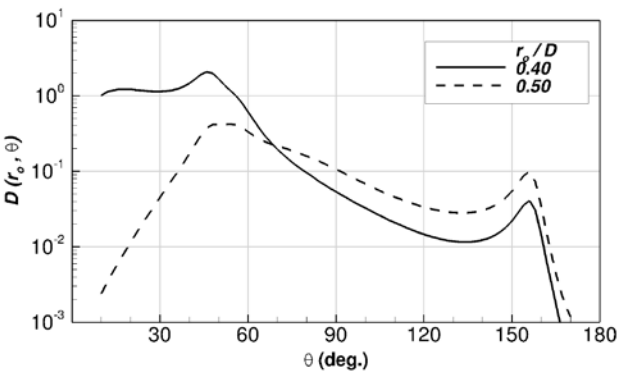

Figure 19. As in figure 18, but with a lined center-body $\bar{Z} = (0.50, 0.50)$.

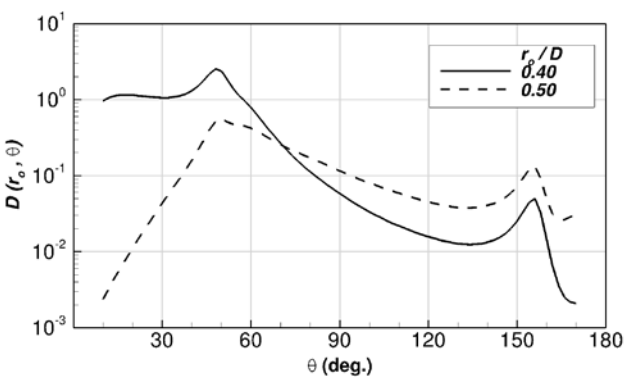

Figure 20. As in figure 18, but in absence of center-body.

Directivity calculations for selective ring sources at radii r_o/D of *0.40* and *0.50* are shown in figures 18 through 20 using flow definitions of figure 5.

At the inner source location of $r_o/D = 0.40$, the flow is supersonic ($U/c_\infty = 1.18$) and the GF is highly directive with a distinct peak near 47°. The flight factor $M_\infty = 0.30$ tends to moderate this peak relative to the static case. This is due to the observation that source radiation angle θ^s is always larger than angle θ (figure 2), thus reducing the peaky appearance of factor $1/(1 - M\cos\theta^s)$ in the direction of maximum radiation angle.

Under static condition (i.e. $\theta^s = \theta$), factor $(1 - M(r_o)\cos\theta^s)$ in the denominator in Eq. (3.10) becomes singular when $M(r_o) > 1$, such as at point $r_o/D = 0.40$ and with $\theta = 32^o$. The singular behavior of the governing second-order ODE near such a critical point $r_o = r_c$ requires a Frobenius-type series expansion. This generates a logarithmic term in the solution as the indicial equation yields two roots that are separated by an integer factor. The usual process requires carrying out the numerical integration of the ODE to a radius slightly smaller than r_c, and using the Frobenius solution as a bridge to connect to $r > r_c$ outside the critical layer. Goldstein and Leib[27] deal with this singularity by introducing a weakly non-parallel flow analysis.

We now turn our attention to the source point $r_o/D = 0.50$ where the mean flow is subsonic ($U/c_\infty = 0.74$). As seen in figures 18 through 20, the corresponding GF is comparatively less directional. Presence of a liner impedance $\bar{Z} = (0.50, 0.50)$ yields slight attenuation at forward angles of $\theta > 100^o$ (see figure 19) relative to similar findings with a rigid CB as in figure 18. In the absence of a CB (figure 20) the GF exhibits a directivity pattern similar to figure 19, but with subtle differences at forward angles. In comparing figures

18 and 20 it is observed that presence of a rigid CB enhances sound propagation at forward angles relative to an exhaust without a CB – while application of an appropriate liner may reduce this enhancement significantly. This is illustrated more clearly in figure 21 by comparing a rigid CB, and two liners with impedance functions $\bar{Z} = (0.50, 0.50)$ and $\bar{Z} = (0.25, 0.25)$. An attenuation of $\sim 5dB$ near $\theta = 130^o$ is noticeable relative to the rigid surface. In addition, further attenuation of $\sim 2dB$ is realized in the peak radiation direction near 50°.

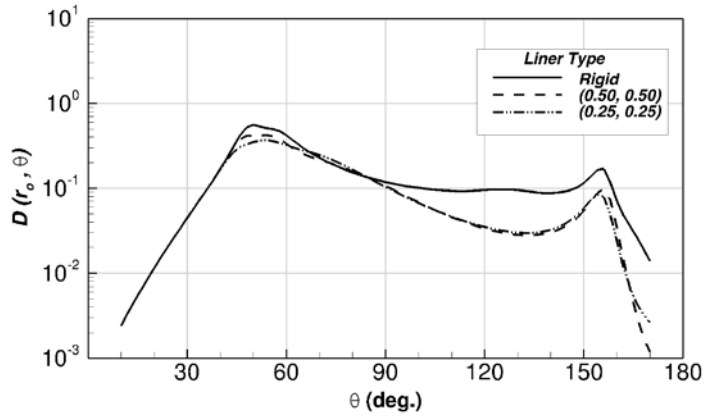

Figure 21. Center-body liner effect on polar directivity of a ring source $(St = 1.0, \eta_o = 0.50)$ at flow definitions of figure 5 $(M_j = 0.90, T_R = 2, M_\infty = 0.30)$: rigid center-body (solid- line); $\bar{Z} = (0.50, 0.50)$ (dashed-line); $\bar{Z}(0.25, 0.25)$ (dash-dotdot).

The effect of ambient Mach number M_∞ on the polar directivity is shown in figures 22 and 23 at $St = 1.0, 0.50$, and subject to a rigid CB. Flight tends to sway the exhaust noise towards the aft angle, as one would expect, and reduce the size of the near-axis zone of relative silence. Additionally, a rigid CB has an amplifying effect on forward radiation in flight at large upstream angles, i.e. $\theta > 150^o$. This is shown in figure 22, and to a larger extend in figure 23 at a lower Strouhal frequency of 0.50. In absence of a CB this forward noise augmentation will weaken significantly under all flight conditions (compare figures 23 and 24 both at $St = 0.50$.)

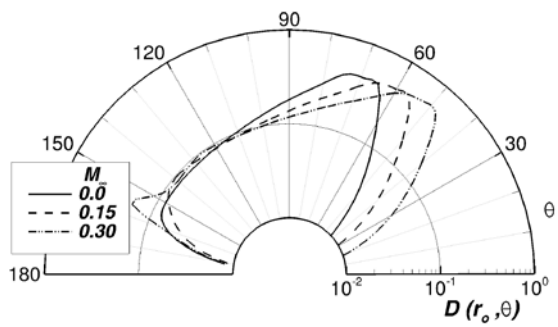

Figure 22. Flight effect on polar directivity due to a ring source $(St = 1.0, \eta_o = 0.50)$ at flow definitions of $(M_j = 0.90, T_R = 2)$ with a rigid center-body at radius $\eta_s = 0.10$: $M_\infty = 0.0$ (solid- line); $M_\infty = 0.15$ (dashed-line); $M_\infty = 0.30$ (dash-dotdot).

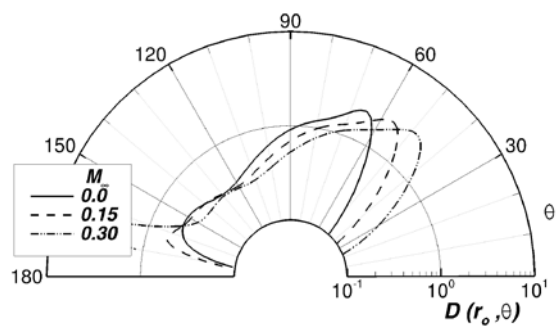

Figure 23. As in figure 22, but at $(St = 0.50)$.

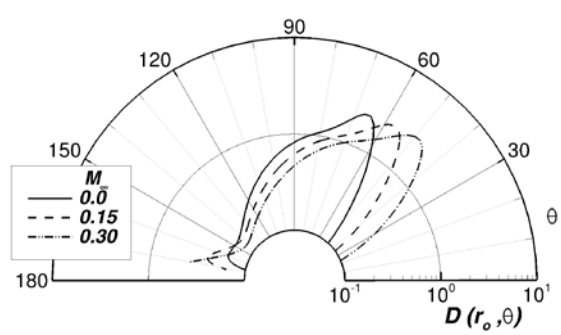

Figure 24. As in figure 23, but in absence of a center-body.

4.2 Downstream the Plug Tip

Shortly downstream of the CB plug-tip the mean velocity profile exhibits a deficit near the centerline as it evolves into a conventional profile further downstream with the disappearance of the wake effect. The mean velocity may be modeled using a slight modification to Eq. (4.3) near the centerline

$$\frac{U(\eta)}{U_j} = \begin{cases} 1 - d_o \operatorname{sech}\left(\frac{\eta}{d_1}\right), & 0 \le \eta < 0.20 \\ \frac{1}{2}\left(1 + \frac{U_\infty}{U_j}\right) - \frac{1}{2}\left(1 - \frac{U_\infty}{U_j}\right)\tanh\big(d_2(\eta - 0.5)\big), & \eta \ge 0.20 \end{cases} \tag{4.8}$$

Parameter $d_o = 0.60$ measures the centerline velocity deficit. Parameters (d_1, d_2) are selected as before in §4.1. The temperature distribution is obtained by substituting (4.8) into Crocco-Busemann law (Eq. 4.4). The centerline values for the mean velocity and static temperature are thus evaluated as $U(0)/c_\infty = 0.472$ and $T(0)/T_\infty = 1.185$ (figure 25). Additionally, the condition of symmetry on the centerline $(\partial U/\partial r = 0)$ is satisfied by the above velocity profile.

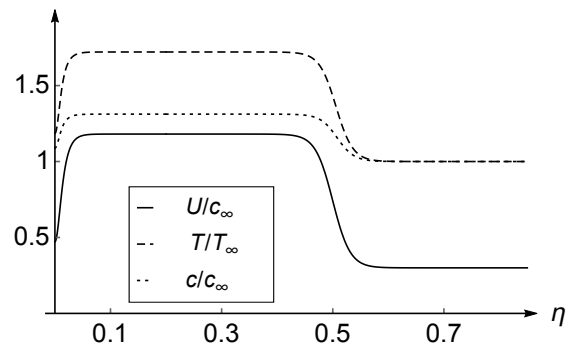

Figure 25. Mean flow profiles downstream of the CB pug-tip: axial velocity (solid line); static temperature (dashed line), and sound speed (dotted line), with $M_j = 0.90, T_R = 2, M_\infty = 0.30$.

The corresponding ring source directivity factor $D(r_o, \theta)$ is shown in figure 26 for a ring at radius $\eta_o = 0.50$, $St = 1.0$, and with M_∞ denoted as a parameter. This figure should be contrasted with figure 22 subject to a rigid CB at local surface radius $\eta_s = 0.10$. The major difference takes place at large forward angles, say $\theta > 110^o$, where figure 26 displays a larger attenuation. Similar results are illustrated in figure 27 at a lower frequency of $St = 0.50$. Again, comparing this result with a related figure in presence of the CB (figure 23) indicates a significant reduction in the GF amplitude at large forward angles, while downstream directivity results effectively remain comparable.

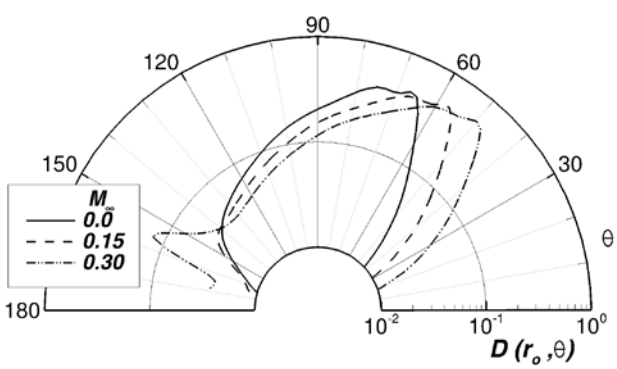

Figure 26. Flight effect on polar directivity due to a ring source $(St = 1.0, \eta_o = 0.50)$ at flow conditions $(M_j = 0.90, T_R = 2)$ aft the CB plug-tip: $M_\infty = 0.0$ (solid- line); $M_\infty = 0.15$ (dashed-line); $M_\infty = 0.30$ (dash-dotdot).

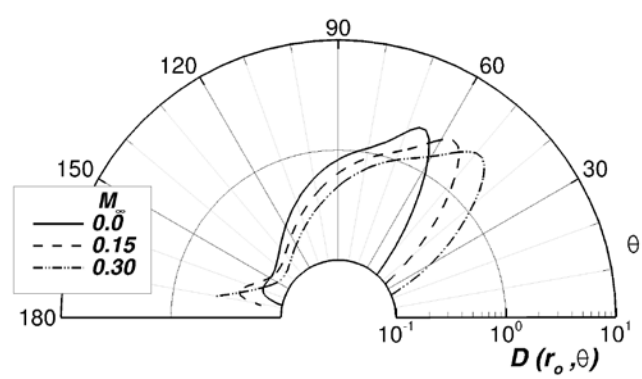

Figure 27. As in figure 26, but at $(St = 0.50)$.

4.3 Surface Boundary Condition – Slip Boundary

Computational fluid dynamic codes normally consider the action of viscosity strong enough to warrant a no-slip, adiabatic, boundary condition on the nearby solid surfaces. When the effect of fluid viscosity at the surface is considered as small, a slip boundary condition could be imposed. Here we examine the propagation GF subject to such a presumption considering that it may be feasible to fashion a boundary with this description.

Appendix A uses Myers[28] boundary condition to derive an equation equivalent to Eq. (2.18) but applicable to a slip boundary. Using Eq. (A5) in place of Eq. (2.18), it is readily shown that function $\psi(k_1, r, \omega, \bar{Z})$ takes the following form when solving for $V_n^{(1)}(r)$ in Eq. (2.24)

$$\psi(k_1, r, \omega, \bar{Z}) = \frac{\left(k_1 \sin\alpha + \frac{c_\infty^2}{c^2}(\kappa_o - k_1 M)/\bar{Z}_1\right)}{i\cos\alpha + \frac{\sin\alpha}{\kappa_o - k_1 M}\left(\frac{\partial M}{\partial r}\right)} + \left(\frac{c^{2\prime}}{2c^2} - \frac{k_1 M'}{-\kappa_o + k_1 M}\right). \qquad \text{(slip boundary)} \qquad (4.9)$$

Factor $\bar{Z}_1$ is related to impedance function $\bar{Z}$ according to Eq. (A6) in Appendix A. Alternatively, when solving the PB equation for $G_n^{(1)}(r)$, the surface condition is expressed as Eq. (C7) in the Appendix where function ψ_1 is defined according to Eqs. (C8) or (C9) for no-slip or slip surfaces, respectively.

In applying a no-slip condition on the surface, one should bear in mind that the continuity equation requires the base flow velocity component normal to the surface, $\tilde{v}_n$, satisfy the condition $\partial\tilde{v}_n/\partial\xi_n = 0$ where coordinate ξ_n is normal to the boundary. For a parallel flow, this would imply that $\partial U/\partial r$ should vanish on the CB surface. In practice, however, mean velocity gradient near the surface may not be negligible due to the convergence of jet flow to the centerline along the surface, hence in formulating the no-slip condition term $M'(r)$ was kept in equation (2.21b) even though the model adopted in Eq. (4.3) shows that $M'(r) = 0$ on the surface.

Sample ring-source directivity computations with source definitions ($St = 1.0, \eta_o = 0.50$) are presented here subject to both slip and no-slip surface conditions. The mean velocity profile for a no-slip case was defined in Eq. 4.3. In examining the GF subject to a slip boundary, the velocity profile outside the wall BL is defined as before, however the near-wall profile in Eq. 4.3 is now modified

$$\frac{U(\eta)}{U_j} = \tanh\left(\frac{\eta - \eta_s + d_o}{d_1}\right). \qquad \eta_s \le \eta < 2\eta_s + \delta_w \qquad (4.10)$$

Parameters $d_o = 1.0 \times 10^{-2}$ and $d_1 = 2.5 \times 10^{-2}$ govern the slip velocity as $U(\eta_s)/U_j = \tanh(d_o/d_1)$, and the boundary layer thickness as $\delta_w = -d_o + 2.646 d_1$. Two impedance values are examined here: *rigid* and $\bar{Z} = (0.50, 0.50)$. For the rigid surface, figure 28 shows that a slip boundary condition works to reduce forward propagation by as much as $\sim 4dB$ near $\theta = 130^o$, while for a lined surface a slip boundary condition has the opposite effect of increasing the noise by 1 to $2dB$ throughout the polar angles as seen in figure 29.

These simulations indicate that a no-slip boundary, when coated with a liner with suitable impedance characteristics, has the most noise-reduction potential – with the promise to attenuate noise from sources near the nozzle exit and/or in the proximity of an external center-body. This is best illustrated in figure 21, and presents the main result of this study.

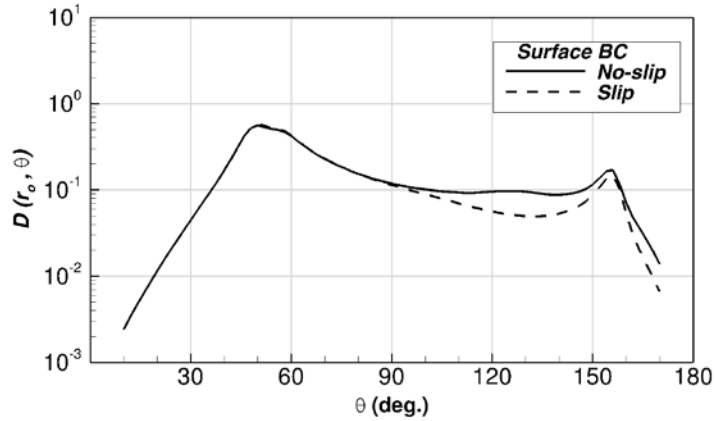

Figure 28. Effect of center-body surface condition on polar directivity of a ring source ($St = 1.0, \eta_o = 0.50$) at flow definitions ($M_j = 0.90, T_R = 2, M_\infty = 0.30$) using a rigid center-body: *no-slip BC* (solid line); *slip BC* (dashed line).

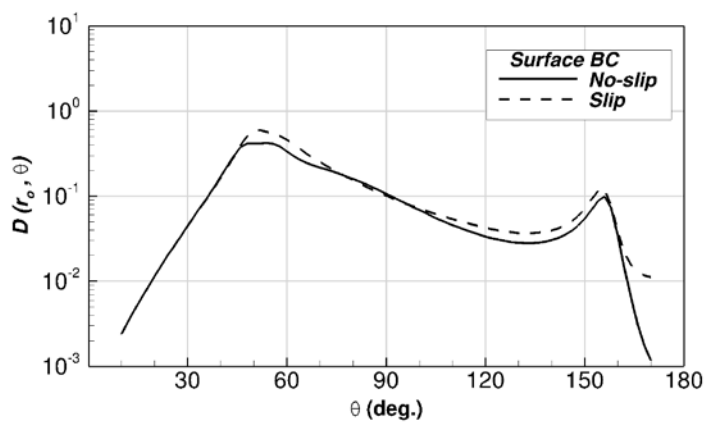

Figure 29. As in figure 28, but using a center-body with impedance $\overline{Z} = (0.50, 0.50)$

5. Summary

The Green's function solution to the compressible Rayleigh equation, applicable to a turbofan jet engine exhaust, and subject to appropriate conditions on the center-body and flight condition in the ambient was discussed. This GF may be implemented in conjunction with fan or jet noise sources in an attempt to assess the far-field engine exhaust noise, its directivity, and spectra. While sources associated with the jet mixing noise are distributed throughout the mixing layer, and up to 20–diameters from the exhaust, fan-related noise sources (broad-band and tone noise) may to be defined as a distribution of equivalent pressure-like sources at the engine exhaust. Thus, in the context of a locally parallel mean flow, velocity and temperature profiles at the exhaust plane are considered as the representative of the shear flow associated with the fan noise GF.

Two forms of the reduced wave-equation (Eq. 2.22 and C3) were discussed, and the exact solutions to the governing initial value problems were produced. Hyperbolic functions were deployed to represent the mean velocity profile. The static temperature profile was modeled after Crocco-Busemann law at a temperature ratio of 2.0 and acoustic Mach number $U_j/c_\infty = 1.18$. Sample GF calculations were presented as a function of boundary conditions on the center-body, flight Mach number, and at selective source locations and frequency. The ratio of the two GF solutions was shown to be unity at any mode number (Eq. 4.6). It was also argued that the PB equation is computationally advantageous due to lower order derivatives present in discretizing the mean flow.

When assessing the significance of source/observer azimuthal separation $\Delta\phi$ on the amplitude of a point source GF, it was shown (figures 15 to 17) that the GF associated with $\Delta\phi = 0$ dominates the one associated with $\Delta\phi = \pi$ at aft polar angles, whereas at forward angles the opposite was true. In examining a ring source directivity factor (assuming azimuthally compact sources) it was shown in figure 21 that a reduction of $\sim 5.0dB$ in amplitude may be achieved at forward angles, near $\theta = 130^o$, provided that the center-body is treated with an appropriate impedance liner.

The impact of flight on a ring source directivity factor indicates that (figures 22 to 24) while an increase in the flight Mach number sways the noise towards the down-stream axis, it also has the unexpected consequence of increasing the noise amplitude at forward angles, $\theta > 150^o$, and with a stronger impact at low frequency.

NOMENCLATURE

α	center-body cone angle.
b_n	Far-field amplitude (Eq. 2.15c)
c	Sound speed
D	Jet nominal diameter
$D(r,\theta)$	Ring source directivity (Eq. 4.7)
δ_w	Normalized boundary layer thickness
$\phi, \Delta\phi$	Azimuthal angle; Source/observer azimuthal separation
η	Normalized radial distance r/D
G	Green's function
$\hat{G}, \breve{G}$	Transformed Green's function
G_N	Normalized Green's function
Γ	Source
k_1	Stream-wise wave number component
k_1^*	Stream-wise wave – stationary phase solution ($\kappa_o \cos\theta^s$)
κ_o	Wave number magnitude (ω/c_∞)
M	Acoustic Mach number (U/c_∞)
ω	Radian frequency $(2\pi f)$
π'	Normalized pressure fluctuation
p'	Acoustic pressure fluctuation
ρ	Density
R	Distance $\lvert\vec{x}-\vec{y}\rvert$
St	Strouhal frequency ($f\ D/U_j$)
ψ	Surface condition (Eq. 2.21b)
ψ_1	Surface condition (Eq. C7)
Ψ	Flight factor (Eq. 3.9)
t	Observer time
T_R	Stagnation temperature ratio
τ	Source time
U	Mean axial velocity
v_i'	Fluctuating velocity component
$\tilde{\boldsymbol{v}}$	Base flow velocity vector
θ	Polar angle (from down-stream axis)
θ^s	Radiation angle (Eq. 3.7)
W	Wronskian
$\vec{x}$	Dependent variable
$\vec{y}$	Source variable
$\bar{Z}$	Normalized surface impedance

Subscripts

$_o$	At the source
∞	Ambient condition
j	Exhaust condition
s	At the center-body

Superscripts

$\hat{}$, $\breve{}$	Fourier transformed variable

Appendix A – Slip Boundary Condition on the Center-Body

For slip-type boundary, the tangential component of the mean velocity on the surface does not vanish. It is shown by Myers[28] that the fluctuating velocity component normal to a bounding surface, for a time harmonic oscillation $\exp(-i\omega t)$, is related to the pressure fluctuations $p'(\omega)$ and the complex surface impedance $Z(\omega)$ as

$$v'_{\perp}(\omega) = -\frac{p'}{Z} + \frac{1}{i\omega Z}\tilde{\boldsymbol{v}}.\nabla p' - \frac{p'}{i\omega Z}\vec{n}.(\vec{n}.\nabla\tilde{\boldsymbol{v}}). \qquad \text{(on the surface)} \tag{A1}$$

When imposing a no-slip condition $\tilde{\boldsymbol{v}} = 0$, the continuity equation yields $\vec{n}.\nabla\tilde{\boldsymbol{v}} = 0$ on the surface, which leads to the standard result $v'_{\perp}(\omega) = -\frac{p'}{Z}$.

Using $\vec{n} = \sin\alpha\,\vec{\imath} + \cos\alpha\,\vec{\jmath}$ as the outward unit normal to the surface of the conical center-body, and $\tilde{\boldsymbol{v}} = U(r)\,\vec{\imath}$ as the base-flow mean velocity (locally parallel) we find $\vec{n}.\nabla\tilde{\boldsymbol{v}} = (\frac{\partial U}{\partial r}\cos\alpha)\vec{\imath}$, subsequently

$$v'_{\perp} = -\frac{p'}{Z} + \frac{1}{i\omega Z}\left(U\frac{\partial p'}{\partial x_1} - \sin\alpha\,\cos\alpha\,\frac{\partial U}{\partial r}\,p'\right). \tag{A2}$$

Further, a locally reactive surface impedance is independent of the position, and a Fourier transform with respect to the stream-wise direction x_1 yields

$$\hat{v}'_{\perp} = -\frac{\hat{p}'}{Z} + \frac{1}{i\omega Z}(i\,k_1 U - \sin\alpha\,\cos\alpha\,\frac{\partial U}{\partial r})\,\hat{p}'. \tag{A3}$$

Using the above result in the momentum equation

$$\frac{\partial p'}{\partial x_j} + \left(\frac{\partial}{\partial t} + U\frac{\partial}{\partial x_1}\right)(\rho v'_j) + \delta_{j1}\left(\rho v'_l\frac{\partial U}{\partial x_l}\right) = 0, \tag{A4}$$

and noting that $\rho = \rho(r)$, one can show the surface condition subject to a slip boundary

$$-i\left(k_1\sin\alpha + \frac{\rho}{Z_1}(\omega - k_1 U)\right)\hat{p}' = \left(\cos\alpha - \frac{i\sin\alpha}{\omega - k_1 U}\frac{\partial U}{\partial r}\right)\frac{\partial\hat{p}'}{\partial r}, \quad \text{(on the surface)} \tag{A5}$$

where

$$\frac{1}{Z_1} = \frac{1}{Z}\left(1 - \frac{1}{i\omega}(i\,k_1 U - \sin\alpha\,\cos\alpha\,\frac{\partial U}{\partial r})\right). \tag{A6}$$

The equivalent no-slip surface condition was given by Eq. (2.18).

Appendix B – Vanishing of the Surface Integral

It can be shown that the boundary condition stated in Eq. (2.21) eliminates the surface integrals (due to the center-body) from the Green's function formulation of the acoustic field in a bounded media. To demonstrate this, we start with Eq. (2.1), and apply Fourier transforms with respect to variables x_1 and t. As before, a circumflex denotes a FT variable according to Eq. (2.5)

$$(\nabla_T^2 + f(k_1, \vec{x}_T, \omega))\hat{\vartheta} = \hat{\Lambda}(k_1, \vec{x}_T, \omega)\,. \tag{B1}$$

Function f is defined in Eq. (2.9), and $\widehat{\Lambda}$ is related to the transform of the source term Γ

$$\hat{\vartheta}(k_1,\vec{x}_T,\omega) \equiv \frac{c(\vec{x}_T)}{-\omega+k_1U(\vec{x}_T)}\,\widehat{\pi}'(k_1,\vec{x}_T,\omega), \qquad \widehat{\Lambda} \equiv \frac{i}{c(\vec{x}_T)\left(-\omega+k_1U(\vec{x}_T)\right)^2}\,\hat{\Gamma} \tag{B2}$$

We multiply Eq. (B1) by $\breve{G}$, and Eq. (2.7) by $\hat{\vartheta}$, subtract the two expressions, and integrate the result on a span-wise plane surrounding the plug surface, and extending to the far field (figure B1). The discussion obviously does not depend on the geometry of the plug cross-section, shown here as the shaded region enclosed by contour "C_1". Therefore

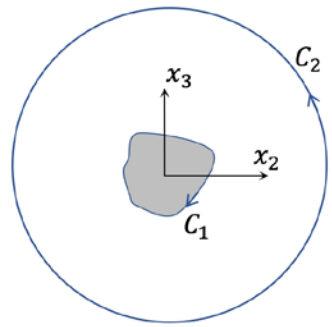

Figure B1. Integration contour in a span-wise plane surrounding the center-body.

$$\int_{\vec{x}_T}\left(\left(\nabla_T^2\breve{G}+f(k_1,\vec{x}_T,\omega)\breve{G}\right)\hat{\vartheta}-\left(\nabla_T^2\hat{\vartheta}+f(k_1,\vec{x}_T,\omega)\hat{\vartheta}\right)\breve{G}\right)d\vec{x}_T = \int_{\vec{x}_T}\left(\delta(\vec{x}_T-\vec{y}_T)\hat{\vartheta}-\breve{G}\,\widehat{\Lambda}\right)d\vec{x}_T. \tag{B3}$$

Area integration $d\vec{x}_T = dx_2dx_3$ spans the region between contours "C_1" and "C_2". Upon using Green's Lemma, the LHS of Eq. (B3) is converted into a path integral surrounding this area

$$-\oint_C\left(\hat{\vartheta}\,\frac{\partial\breve{G}}{\partial\vec{n}}-\breve{G}\,\frac{\partial\hat{\vartheta}}{\partial\vec{n}}\right)ds = \hat{\vartheta}(k_1,\vec{y}_T,\omega)-\int_{\vec{x}_T}\breve{G}(k_1,\vec{x}_T|\,\vec{y}_T,\omega)\widehat{\Lambda}(k_1,\vec{x}_T,\omega)d\vec{x}_T\,, \tag{B4}$$

where contour "C" = "C_1" + "C_2" is shown in figure B1, $\vec{n}$ is the outward normal to the contour, and s denotes the arc increment along the path. Since the GF $\breve{G}$ is self adjoint we switch $\vec{x}_T$ and $\vec{y}_T$ in the argument of $\breve{G}$, and susequently substitute for $\breve{G}$ in terms of $\hat{G}$ from Eq. (2.8), and for $\widehat{\Lambda}$ in terms of $\hat{\Gamma}$ from Eq. (B2) to show that the RHS of Eq. (B4) converts to

$$\frac{c(\vec{y}_T)}{-\omega+k_1U(\vec{y}_T)}\left(\widehat{\pi}'(k_1,\,\vec{y}_T,\omega)-(2\pi)^2\int_{\vec{x}_T}\hat{G}(k_1,\,\vec{y}_T|\vec{x}_T,\omega)\hat{\Gamma}(k_1,\vec{x}_T,\omega)d\vec{x}_T\right).$$

This expression is identically zero as seen from Eq. (2.19). Now letteing the LHS of Eq. (B4) be equal to zero would provide the desired boundary condition. Since the integrand approaches zero on the outer path "C_2" as $r\to\infty$, then inner path integral

$$\oint_{C_1}\left(\hat{\vartheta}\,\frac{\partial\breve{G}}{\partial\vec{n}}-\breve{G}\,\frac{\partial\hat{\vartheta}}{\partial\vec{n}}\right)ds,$$

would vanish only if the integrand is forced to vanish at all points on "C_1"

$$\hat{\vartheta}\,\frac{\partial\breve{G}}{\partial n}-\breve{G}\,\frac{\partial\hat{\vartheta}}{\partial n}=0. \qquad \text{(on the surface)} \tag{B5}$$

Next, we substitue for $\hat{\vartheta}$ in terms of $\widehat{\pi}'$ from Eq. (B2), and impose the surface condition on $\widehat{\pi}'$ according to Eq. (2.18) to obtain the requied boundary condition

$$\frac{\partial \breve{G}}{\partial n} - \psi \breve{G} = 0, \qquad \text{(on the surface)} \tag{B6}$$

where function $\psi(k_1, \omega, \bar{Z})$ is given by Eq. (2.21b) subject to no-slip BC on a conical-shaped center-body.

Appendix C –Alternative form of the Green's Function Solution

A numerical discretization of Eq. (2.22) would require second-order derivatives of the mean velocity and temperature as seen in Eq. (2.11). It is computationally advantageous if these derivatives were kept to a lower order. Using the transformation

$$V_n^{(j)}(k_1, r, \omega) = \beta(k_1, r, \omega) g_n^{(j)}(k_1, r, \omega), \qquad j = 1,2 \tag{C1}$$

$$\beta(k_1, r, \omega) \equiv \frac{c(r)}{-\omega + U(r) k_1}. \tag{C2}$$

in Eq. (2.22) shows that the newly defined function $g_n^{(j)}$ is governed by

$$\left(\frac{d^2}{dr^2} + \left(\frac{1}{r} + \frac{c^{2\prime}}{c^2} - \frac{2k_1 U'}{-\omega + U k_1}\right)\frac{d}{dr} + \frac{(-\omega + U k_1)^2}{c^2} - k_1^2 - \frac{n^2}{r^2}\right) g_n^{(j)}(k_1, r, \omega) = 0\,, \tag{C3}$$

commonly referred to as the Pridmore-Brown equation[23]. Solutions $g_n^{(j)}$ and $V_n^{(j)}$ are related as $r\, W\left(V_n^{(1)}, V_n^{(2)}\right) = r\beta^2\, W\left(g_n^{(1)}, g_n^{(2)}\right)$, Since the two sides of this equation are independent of distance r , it is readily shown that Eq. (2.23a) can now be written as

$$\breve{G}_n(k_1, r|r_o, \omega) = \frac{1}{2\pi r_o}\frac{\beta(k_1, r, \omega)}{\beta(k_1, r_o, \omega)}\frac{g_n^{(2)}(r) g_n^{(1)}(r_o)}{W\left(g_n^{(1)}, g_n^{(2)}\right)_{r=r_o}}\,, \qquad r > r_o \tag{C4}$$

resulting in a modified form of Eq. (3.3)

$$Q_n(r|r_o, \omega) = \frac{c(r_o)}{c_\infty}\int_{-\infty}^{\infty}\frac{\left(-\omega + k_1 U(r)\right)^2}{\left(-\omega + k_1 U(r_o)\right)^3} g_n^{(1)}(k_1, r_o, \omega)\Lambda(g_n^{(1)}, H_n^{(1)})\frac{1}{\sqrt{\chi_\infty}} e^{ir\Theta} dk_1, \tag{C5}$$

where factor $\Lambda\left(g_n^{(1)}, H_n^{(1)}\right)$ is evaluated according to Eq. (3.5), but with $g_n^{(1)}$ substituted for $V_n^{(1)}$. Placing the stationary phase solution to the above integral into Eq. (3.2) yields the desired GF

$$G(\vec{x}, \vec{y}; \omega) \sim \frac{-1}{4\pi^3}\frac{1}{c_\infty^3}\frac{e^{i\kappa_o R\Psi}}{\kappa_o R}\frac{(1 - M_\infty \cos\theta^s)^2}{(1 - M(r_o)\cos\theta^s)^3}\frac{1}{\sqrt{1 - M_\infty^2 \sin^2\theta}}$$

$$\times \sum_{n=0}^{\infty} \varepsilon_n e^{-i\frac{n\pi}{2}} \cos(n\phi)\, g_n^{(1)}(k_1^*, r_o, \omega)\, \Lambda(g_n^{(1)}, H_n^{(1)})\Big|_{k_1 = k_1^*}. \tag{C6}$$

The numerical solution to Eq. (C3) utilizes the following initial conditions at the starting point on the surface

$$\begin{cases} g_n^{(1)}(r) = 1, \\ \frac{\partial}{\partial r} g_n^{(1)}(r) - \psi_1 g_n^{(1)}(r) = 0, \end{cases} \qquad r = r_s \tag{C7}$$

where, on considering a no-slip condition on the plug surface, we find

$$\psi_1(k_1, r, \omega, \bar{Z}) = \frac{-i}{\cos\alpha}\left(k_1 \sin\alpha + \frac{\kappa_o}{\bar{Z}}\frac{c_\infty^2}{c^2}\right). \qquad \text{(no-slip boundary)} \tag{C8}$$

In a slip-type boundary, the pressure fluctuation on the surface is governed by Eq. (A5) as noted in Appendix A. It is straightforward to show that function ψ_1 should now take the form

$$\psi_1(k_1, r, \omega, \bar{Z}) = \frac{\left(k_1 \sin\alpha + \frac{c_\infty^2}{c^2}(\kappa_o - k_1 M)/\bar{Z}_1\right)}{i\cos\alpha + \frac{\sin\alpha}{\kappa_o - k_1 M}\left(\frac{\partial M}{\partial r}\right)}, \qquad \text{(slip boundary)} \tag{C9}$$

where the impedance function $\bar{Z}_1$ is related to $\bar{Z}$ according to Eq. (A6) in Appendix A.

Downstream of the plug tip, the centerline conditions for $g_n^{(1)}$ are similar to those for $V_n^{(1)}$ as stated in Eq. (2.12).

Acknowledgements

Support by the acoustics branch at NASA Glenn Research Center, and the Advanced Air Transport Technology (AATT) project under NASA Advanced Air Vehicle Program, is greatly appreciated. The author is also grateful to Drs. S. J. Leib and L. S. Hultgren, acoustics branch at NASA Glenn Research Center, for their constructive remarks.

References

[1] Goldstein, M. E., "A generalized acoustic analogy," J. Fluid Mechanics, **488**, (2003), pp. 313-333.

[2] Goldstein, M. E., "Relation between the generalized acoustic analogy and Lilley's contribution to aeroacoustics," International J. Aeroacoustics, **9** (4, 5), (2010), pp. 401-418.

[3] Davies, P. O. A. L., Fisher, M. J., and Barratt, M. J., "The characteristic of turbulence in the mixing region of a round jet," J. Fluid Mechanics, **15**, (1963), pp. 337-367.

[4] Chu, W. T., "Turbulence measurements relevant to jet noise," UTIAS Report No. 119, University of Toronto, Nov. 1966.

[5] Doty, M. J. and McLaughlin, D. K., "Space-time correlation measurements of high-speed axisymmetric jets using optical deflectometry," Experiments in Fluids, **38** (4**)**, (2005), pp. 415-425.

[6] Bridges, J., and Wernet, M. P. "Measurements of acoustic sound source in hot jets," AIAA Paper 2003-3130, 2003.

[7] Wernet, M. P. "Temporally resolved PIV for space-time correlations in both cold and hot jet flows," Measurement Science and Technology, **(18)**, (2007), pp. 1387-1403.

[8] Morris, P. J., and Zaman, K. B. M. Q., "Two component velocity correlations in jets and noise source modeling," AIAA paper 2010-3781, 2010.

[9] Tam, C. K. W., and Laurent, A., "Jet mixing noise from fine-scale turbulence," AIAA Journal, **37** (2), (1999), pp. 145-153.

[10] Tam, C. K. W., "Fine scale turbulence noise from dual stream jets," AIAA paper 2004-2871, 2004.

[11] Morris, P. J., Boluriaan, S., Lilley, G. M., and Long, L. N., "Two-point cross correlations of turbulence and noise predictions: Analysis and simulation," AIAA paper 2002-0071, 2002.

[12] Leib, S. J., and Goldstein, M. E., "Hybrid source model for predicting high-speed jet noise," AIAA Journal, **49** (7), (2011), pp. 1324-1335.

[13] Leib, S. J., "Noise predictions for rectangular jets using a conformal mapping method," AIAA Journal, **51** (3), (2013), pp. 721-737.

[14] Khavaran, A., Kenzakowski, D. C., and Mielke-Fagan, A. F., "Hot jets and sources of jet noise," Intl J. Aeroacoustics, **9** (4,5), (2010), pp. 491-532.

[15] Tam, C. K. W., and Auriault, L., “Mean flow refraction effects on sound radiated from localized sources in a jet,” J. Fluid Mechanics, **370**, (1988), pp. 149-174.
[16] Campos, L.M.B.C., and Kobayashi, M. H., “On the propagation of sound in high-speed non-isothermal shear flow,” Intl J. Aeroacoustics, **8** (3), (2009), pp. 199-230.
[17] Wundrow, D. W., and Khavaran, A., “On the applicability of the high-frequency approximations to Lilley’s equation,”J. Sound & Vib., **272**, (2004), pp.793-830.
[18] Brambley, E. J., Darau, M., and Rienstra, S. W., “The critical layer in linear-shear boundary layers over acoustic linings,” J. Fluid Mechanics, **710**, (2012), pp. 545-568.
[19] Gaffney, J., McAlpine, A., and Kingan, M. J., “Fuselage boundary-layer refraction of fan tones radiated from an installed turbofan aero-engine,” J. Acoust. Soc. Am. **141** (3), (2017), pp. 1653-1663.
[20] Chandiramani, K. L., “Diffraction of evanescent waves, with application to aerodynamically scattered sound and radiation from unbaffled planes,” J. Acoustical Soc. Am. **55** (1), (1974), pp. 19-29.
[21] Amiet, R. K., “Noise due to turbulent flow past a trailing edge,” J. Sound & Vib., ***47*** (3), (1976), pp. 387-393.
[22] Lyu, B., Dowling, A. P., and Nagavi, I., “Prediction of installed jet noise,” J. Fluid Mechanics, **811**, (2017), pp. 234-268.
[23] Pridmore-Brown, D. C., “Sound propagation in a fluid flowing through an attenuating duct,” J. Fluid Mechanics, **4**, (1958), pp. 393-406
[24] Hanson, D. B., “Shielding of prop-fan cabin noise by the fuselage boundary layer,” J. Sound & Vib., ***92*** (4), (1984), pp. 591-598
[25] Tennekes, H., and Lumley, J. L., *A First Course in Turbulence* (1972), M.I.T. Press.
[26] Goldstein, M. E. and Leib, S. J., “Azimuthal source non-compactness and mode coupling in sound radiation from high-speed axisymmetric jets,” AIAA paper 2016-2803, 2016.
[27] Goldstein, M. E. and Leib, S. J., “The aeroacoustics of slowly diverging supersonic jets,” J. Fluid Mechanics, **600**, (2008), pp. 291-337.
[28] Myers, M. K., “On the acoustic boundary condition in the presence of flow,” J. Sound & Vib., ***71*** (3), (1980), pp. 429-434.